Two views on dust: polarized thermal dust emission and near-infrared scattering

V.-M. Pelkonen [1], M. Juvela [1], P. Padoan [2], K. Mattila [1]

ABSTRACT

In the first part, we present some results of our ongoing modelling of the polarized thermal dust emission from cloud cores. In our radiative transfer calculations we record the direction-dependence of the incoming radiation, thus allowing us to calculate the anisotropy of the radiation, which should play a major part in the efficiency of the radiative torques. Radiative torque mechanism is widely considered to be a quite promising explanation for the grain alignment in clouds. In addition to the anisotropy, we show the derived polarization map and compare our results with previous studies.

In the second part, we discuss the use of near-infrared diffuse surface brightness maps, arising from scattered light, as a tracer of dust column density in clouds with $A_{\rm V}$ in the range $1 - 15^m$. We present our SOFI NTT -observations of a quiescent filament in the Corona Australis molecular cloud, and compare the derived dust column densities to the result derived from the extinction of the background stars.

Subject headings: galaxies: ISM — infrared: ISM — ISM: dust, extinction — ISM: structure

1. Dust polarization in MHD simulations

1.1. Introduction

One of the most useful methods of gaining information on interstellar magnetic fields is the polarized thermal dust emission, which arises from the alignment of the spin axis of the

[1]Observatory, University of Helsinki, P.O. Box 14, SF-00014 University of Helsinki, Finland

[2]Department of Physics, University of California, San Diego, CASS/UCSD 0424, 9500 Gilman Drive, La Jolla, CA 92093-0424

dust grains along the magnetic field. The main question with dust polarization is the alignment mechanism: what makes the dust grains spin up in the first place? One of the strongest candidates as the primary mechanism of grain alignment is the radiative torque mechanism, where the momentum is transferred by collisions of photons onto the grain, causing a torque which makes the grain rotate around its axis. It was first introduced by Dolginov (1972) and Dolginov & Mytrophanov (1976), and its efficiency has been demonstrated using numerical simulations by Draine & Weingartner (1996).

Cho & Lazarian (2005) used a spherically symmetric model cloud to calculate the size of grains aligned by radiative torques, assuming constant anisotropy factor $\gamma = 0.7$ and neglecting the isotropic component of the radiation. Their calculations showed that even deep inside GMCs ($A_{\rm V} \sim 10^m$), large grains can be aligned by radiative torques. Cho & Lazarian (2005) presented an empirical formula for the minimum size of the aligned grain a_{alg} as a function of the density n_H and extinction $A_{\rm V}$, $a_{\rm alg} = (log\ n_{\rm H})^3(A_{\rm V,1D}+5)/2800\ \mu$m. This formula is, strictly speaking, only valid for smooth spherical clouds, and carries the additional assumption of a constant anisotropy factor $\gamma = 0.7$. Pelkonen et al. (2007) modelled polarization in a clumpy cloud using this formula as a first approximation.

A more detailed study of the anisotropy inside a clumpy cloud is done by Bethell et al. (2007), who found the average anisotropy factor to be 0.34. However, their results did not change the qualitative results of Cho & Lazarian (2005). As a continuation of our own previous paper (Pelkonen et al. 2007), we are conducting a similar study of the anisotropy vector γ and calculating the minimum sizes of the aligned grains within our model clouds. In addition to calculating 1D models to compare with Eq. 1, we also show the comparisons with our previous 3D models (Pelkonen et al. 2007).

1.2. Grain alignment by radiative torques

A grain is aligned with the magnetic field, if its rotation rate due to radiative torques exceeds its thermal rotation rate. This leads to the following formula (see Draine & Weingartner 1996, Cho & Lazarian 2005):

$$\begin{aligned}(\frac{\omega_{rad}}{\omega_T})^2 &= \frac{5\alpha_1}{192\delta^2}\frac{\rho a_{eff}}{m_{\rm H}}(\frac{1}{n_H kT})^2 \\ &\quad \times[\int d\lambda(\mathbf{Q_\Gamma}\cdot\hat{\mathbf{a_1}})\lambda(4\pi J_\lambda/c)]^2(\frac{1}{1+\frac{\tau_{drag,gas}}{\tau_{drag,em}}})^2, \end{aligned} \quad (1)$$

where a_{eff} is the effective grain size, Q_Γ is the radiative torque efficiency (see Fig. 2a), γ is the anisotropy factor, and $\tau_{drag,gas}/\tau_{drag,em}$ is the ratio of gas drag time to thermal emission drag time. Based on Table 4 of Draine & Weingartner (1996), we estimate $Q_{\Gamma,iso} = 0.1Q_{\Gamma,aniso}$.

1.3. Results

As the first test case, we examine a spherically symmetric one solar mass cloud. The density distribution is that of a critically stable Bonner-Ebert sphere. The dust model is taken from Li & Draine (2001). Radiative transfer calculations are used to estimate the radiation field within the cloud (attenuated external radiation plus dust emission), and to calculate its angular distribution within each cloud position.

Figure 2b shows the anisotropy within a 1D model cloud. Note that the intensity of the short wavelength radiation drops sharply with $A_{\rm V}$, while anisotropy tracks only the angular distribution of the remaining intensity. At longer wavelengths the dust emission starts to dominate and the direction of the anisotropy changes towards the surface. When calculating the minimum size of the aligned grains, our results differ from the formula of Cho & Lazarian (2005), needing larger grains. The difference is due to the adoption of an invariant $\gamma = 0.7$ by Cho & Lazarian (2005). Furthermore, the radiation that penetrates deeper into the core is of longer wavelength and less anisotropic, which means it is less efficient in exerting radiative torque on the grains. Thus, the results would diverge even more at high $A_{\rm V}$.

The clumpy 3D cloud is more complex. Instead of a clearly defined direction of highest intensity, the radiation penetrates into the cloud from numerous directions, resulting in a decrease of anisotropy. Figure 3 shows the effect of the calculated anisotropy on polarization. The general morphology in the diffuse region is unchanged, but the depolarization of the cores is more pronounced, as expected from the 1D results. Higher resolution simulations are in progress for a more detailed study of the dense cores.

2. Interstellar cloud seen in NIR scattered light

2.1. Introduction

With the current wide-field instruments the near-infrared (NIR) scattered light can be mapped over large cloud areas. Below $A_{\rm V} \sim 10^m$ the surface brightness is directly proportional to the column density. At somewhat higher column densities, $A_{\rm V} < 20^m$, the saturation of the surface brightness can be corrected using the intensity ratios of the NIR bands. This makes it possible to convert surface brightness measurements into reliable estimates of column density. The main advantage of the method is the high, even sub-arcsecond resolution. The advance of the NIR instrumentation makes this a promising new method for the mapping of quiescent interstellar clouds (see Juvela et al. 2007).

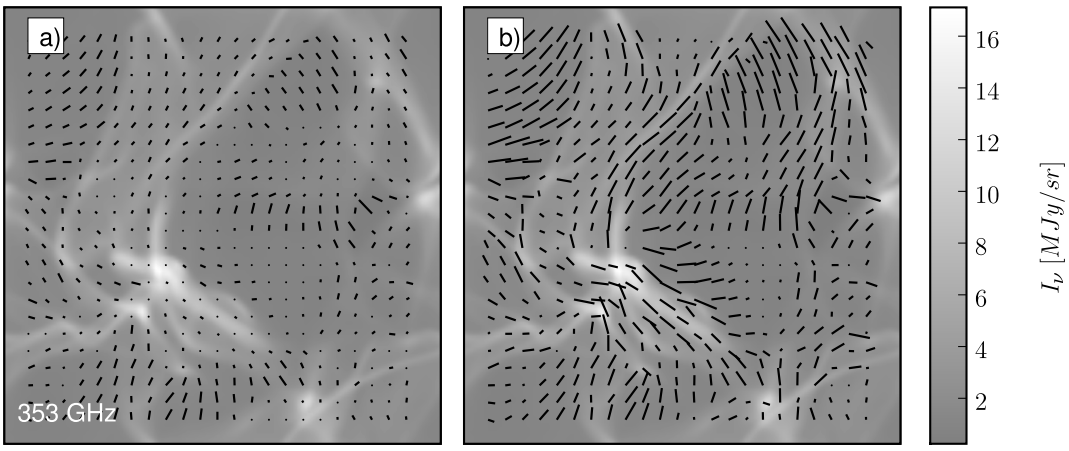

Fig. 1.— A figure of a MHD simulation of an interstellar cloud a few parsecs across from our paper (Pelkonen et al. 2007), in which we used the empirical formula by Cho & Lazarian to estimate the size of the aligned grains. The polarization vectors are drawn for every fifth pixel. The maximum polarization degree is 9% in the left frame and 13% in the right frame. The background grayscale image is the dust emission at 353 GHz. The left frame shows the reduction of polarization towards the cores. In the right frame all grains are assumed to be aligned. In the filaments the visual extinction reaches a few magnitudes.

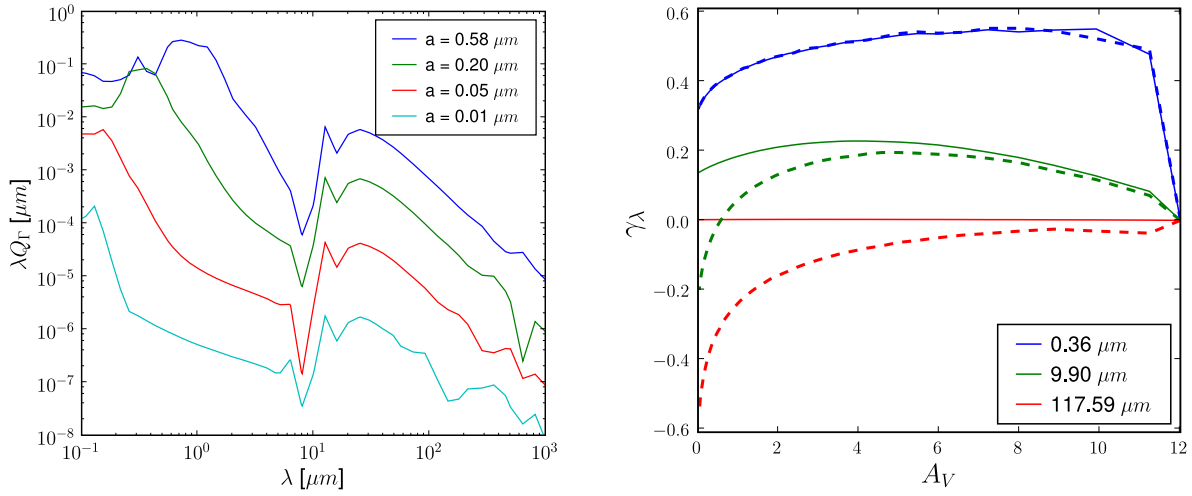

Fig. 2.— On the left is a figure showing interpolated λQ_Γ to various grain sizes, where Q_Γ is the efficiency of the radiative torques. Original data courtesy of J. Cho. The figure shows that short wavelengths are much more efficient in aligning grains. Large grains are also much easier to align. On the right is the anisotropy factors for different wavelengths inside a 1D model cloud. The solid lines is the model without dust emission and the dashed with dust emission.

2.2. Observations of a Corona Australis cloud filament

We have made deep near-infrared observations of a cloud filament in the Corona Australis molecular cloud using the SOFI instrument on the NTT telescope at the ESO observatory of La Silla, Chile. The goal was to detect NIR scattered light towards the cloud and to confirm that this surface brightness can be used to derive reliable column density maps. Figure 4 shows the observed surface brightness in J, H, and Ks bands.

2.3. Column density estimation

The column density estimates were made using methods presented by Padoan et al. (2006) and Juvela et al. (2006). The photometry of the background stars and the NICER method (Lombardi & Alves 2001) were used to derive an independent extinction map.

Padoan et al. (2006) presented formulas for converting scattered surface brightness into dust column density. At low visual extinctions the relationship is linear, but around $A_{\rm V} \sim 10^m$ even NIR surface brightness values begin to saturate. The intensity is assumed to follow a formula $I_\lambda = a_\lambda \times (1 - e^{b_\lambda A_{\rm V}})$. Based on numerical simulations this form is approximately correct as long as saturation remains weak. If J- and H-bands are compared with Ks-band data, $A_{\rm V}$ can be eliminated, $I_\lambda = a_\lambda \times (1 - (1 - I_{\rm K}/a_{\rm K})^{b_\lambda/b_{\rm K}})$. Once parameters have been obtained, extinction estimates are derived from the equation $A_{\rm V} = \left[log(1 - I_\lambda/a_\lambda)\right]/b_\lambda$.

We fit to observations a parametric curve defined by $I_\lambda = a_\lambda \times (1 - e^{b_\lambda A_{\rm V}})$. The minimization of the sum over squared distances of the observed triplets (I_J, I_H, I_{Ks}) from the curve gives values for the parameters a and b. The parameter b_{Ks} is kept constant because observations can be used to fix only the ratio of b-parameters. We use for b_{Ks} a value of 0.125 mag^{-1} obtained from simulations (Juvela et al. 2006).

Figure 5 shows the correlation between the extinctions derived from the surface brightness and the colour excesses of background stars using the NICER method. The two methods agree in their main features and give quantitatively similar $A_{\rm V}$ estimates. At $A_{\rm V} > 15^m$ the scatter increases, which may be due to the NICER values being affected by poor sampling in regions with strong extinction gradients. We examined this possible bias with simulated observations, taking as the starting point the $A_{\rm V}$ map derived with NICER method. Background stars are simulated using the magnitude and intrinsic colour distribution from observations. The synthetic observations are run through the NICER routine, resulting in a new extinction map. The procedure is repeated so that we obtain 100 realizations of the extinction map. In Figure 6 the results are compared with each other and with the input $A_{\rm V}$ distribution, indicating a significant bias.

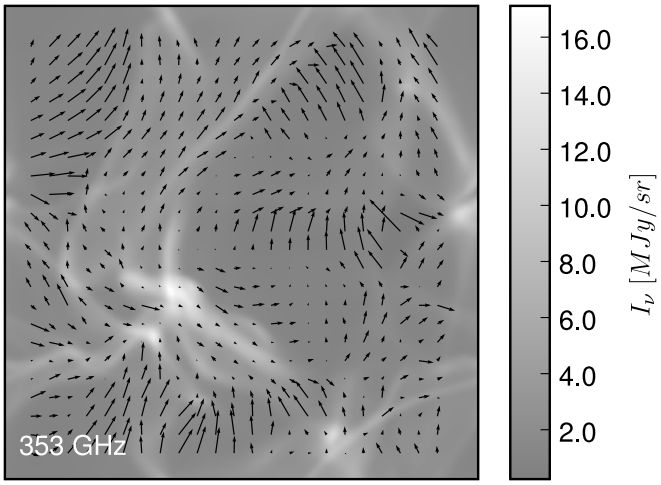

Fig. 3.— A simulated polarization map at 353 GHz. In the calculation we have taken into accound the actual anisotropy of the radiation field that is obtained from simulations. Compared with the assumption of a constant gamma (Fig 1a) the results are morphologically almost identical. There is a drop in overall polarization degree (for example the maximum drops to 7%). The polarization degree decreases even more sharply towards the dense cores.

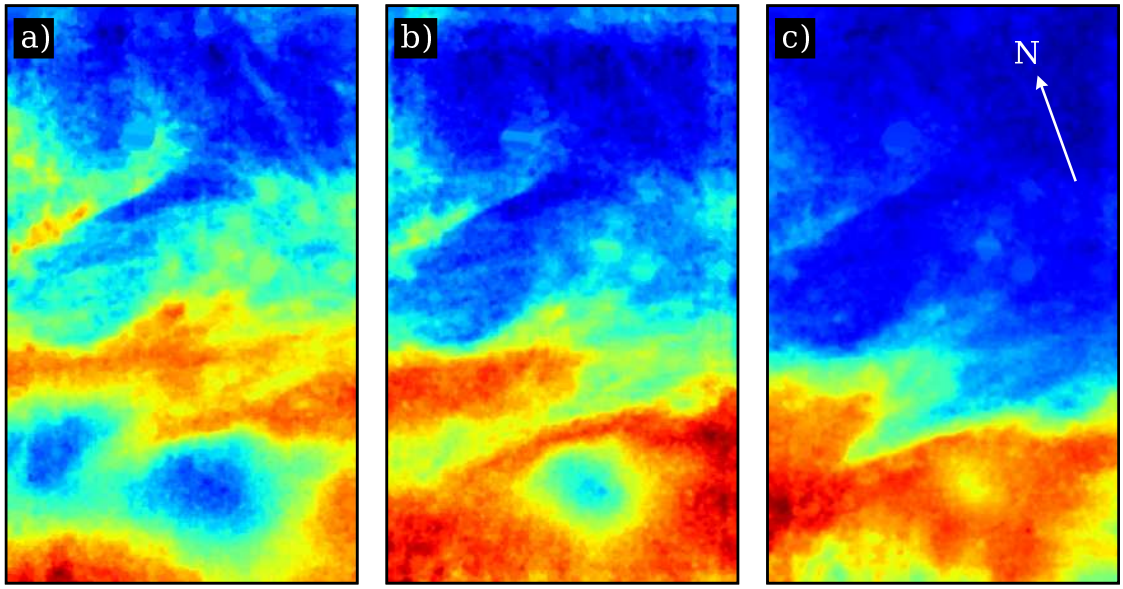

Fig. 4.— Observed surface brightness in J, H, and Ks bands (frames a, b, and c, respectively). In frame c the arrow shows the direction of the equatorial north. The filament runs horizontally through the lower part of the figures. The Ks image is well correlated with the column density, but the shorter wavelengths show clear local minima at the location of the highest optical depth.

2.4. Conclusions

– Surface brightness could be detected over most of the imaged fields where, according to the NICER analysis, the A_V ranges from 1.8^m to more than 30^m.

– The NIR intensities and their A_V dependencies are consistent with the surface brightness being caused by dust scattering. No indication of additional dust emission at low A_V was detected.

– In regions below $A_V \sim 15^m$ the column density estimates derived using scattered light and the colour excesses of background stars agree with each other.

– In the interval $A_V = 15 - 20^m$ the surface brightness data predicts up to 50% higher extinction values than the colour excess method. We interpret this as bias in the colour excess method caused by the strong extinction gradients and the small number of background stars.

– In our case the surface brightness data allow construction of a column density map with resolution a few times better than that provided by the background stars.

REFERENCES

Bethell, T.J., Chepurnov, A., Lazarian, A., & Kim, J. 2007, ApJ, 663, 1055

Cho, J., & Lazarian, A. 2005, ApJ, 631, 361

Dolginov, A. Z. 1972, Ap&SS, 18, 337

Dolginov, A. Z., & Mytrophanov, I. G. 1976, Ap&SS, 43, 291

Draine, B. T., & Weingartner, J. 1996, ApJ, 470, 551

Juvela, M., Pelkonen, V.-M., & Padoan, P. 2006, A&A, 457, 877

Juvela, M., Pelkonen, V.-M., Padoan, P., & Mattila, K. 2007, A&A, in press

Li, A., & Draine, B., 2001, ApJ 554, 778

Lombardi, M., & Alves, I., 2001, A&A, 377, 1023

Padoan, P., Juvela, M., & Pelkonen V.-M. 2006, ApJ, 636, L101

Pelkonen, V.-M., Juvela, M., & Padoan, P. 2007, A&A, 461, 551

This preprint was prepared with the AAS LaTeX macros v5.2.

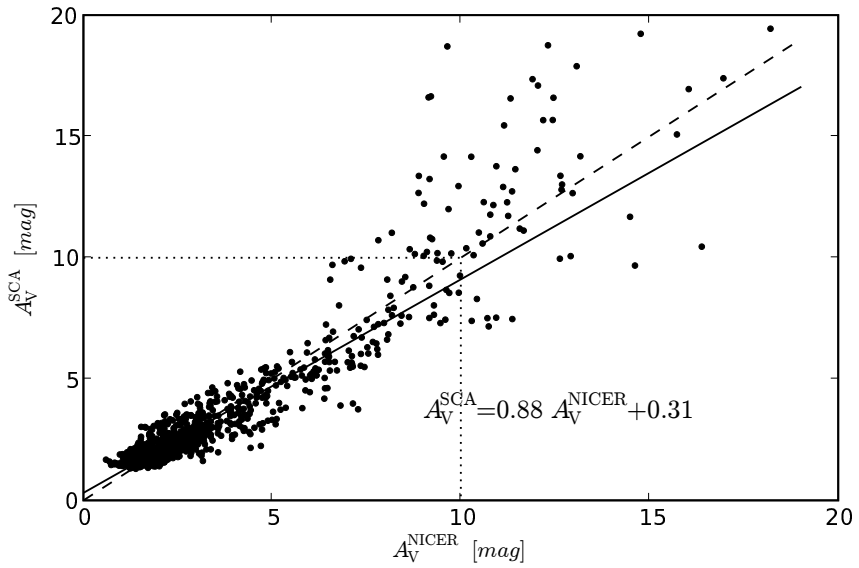

Fig. 5.— Correlation between the extinction derived using the NICER method, A_V^{NICER}, and the values derived from surface brightness measurements, A_V^{SCA}. The comparison is limited to area with A_V below 20^m. The points correspond to 20" pixels.

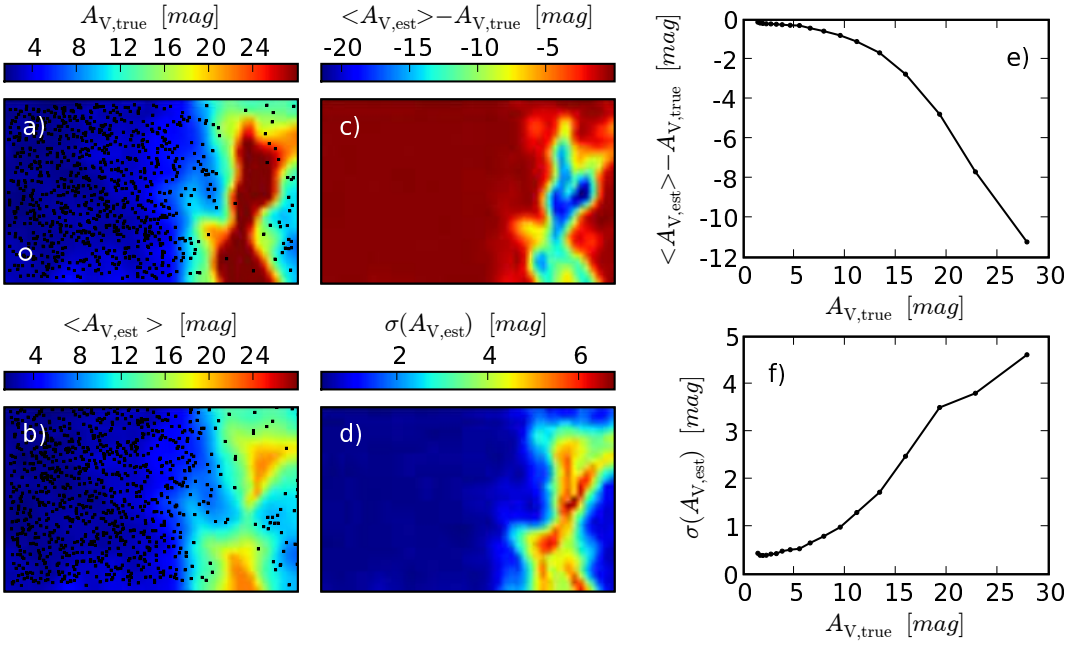

Fig. 6.— Frame a shows the observed stars and the derived extinction map. Assuming this extinction distribution, frame b shows the distribution of stars and the estimated A_V for simulated observations. Based on such simulations, frames c and e show the estimated bias and frames d and f the estimated scatter in the extinction estimates.